ACS OMEGA

Open Access

http://pubs.acs.org/journal/acsodf

Article

Quantification of Uranium in Complex Acid Media: Understanding Speciation and Mitigating for Band Shifts

Heather M. Felmy, Nathan P. Bessen, Hope E. Lackey, Samuel A. Bryan,* and Amanda M. Lines*

Cite This: *ACS Omega* 2023, 8, 41696−41707

Read Online

ACCESS | Metrics & More | Article Recommendations | Supporting Information

ABSTRACT: In situ and real-time analysis of chemical systems, or online monitoring, has numerous benefits in all fields of chemistry. A common challenge can be found in matrix effects, where the addition of a new chemical species causes chemical interactions and changes the fingerprints of other chemical species in the system. This is demonstrated here by looking at the Raman and visible spectra of the uranyl ion within combined nitric acid and hydrofluoric acid media. This system is not only highly important to nuclear energy, a green and reliable option for energy portfolios, but also provides a clear chemistry example that can be applied to other chemical systems. The application of optical spectroscopy is discussed, along with the application and comparison of both multivariate curve resolution and HypSpec to deconvolute and understand speciation. Finally, the use of chemical data science in the form of chemometric modeling is used to demonstrate robust quantification of uranium within a complex chemical system where potential matrix effects are not known *a priori*.

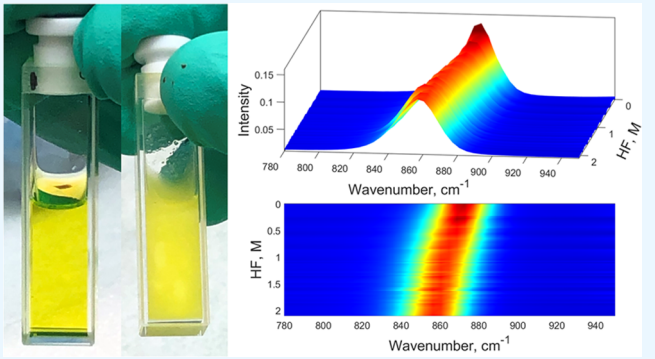

INTRODUCTION

Nuclear energy is notable as a green energy source and a key component of a climate-conscious and reliable energy portfolio.[1−3] By recycling used nuclear fuel, it is possible for nuclear energy initiatives to push closer to a renewable source, improve U.S. energy security, and reduce the volume of waste slated for a geological repository. Various chemical processes for recycling light water reactor fuel are well documented, and new schemes are being developed for fuel anticipated from the next generation of reactors.[4,5] In all of these processes, careful analytical monitoring and control of the process streams and products are required to support accountability and maintain product quality. Integration of online monitoring is an effective way to meet analytical requirements while also allowing for the reduction of sampling costs and optimizing processing speed and safety.

Optical spectroscopy is an ideal tool for online and real-time monitoring of radiochemical processes. Not only are these mature technologies capable of providing insight into the quantity, speciation, and oxidation state of key actinides and transition metals in solution, but they are uniquely well suited to radiological applications. Specifically, techniques such as ultraviolet−visible (UV−vis),[6] fluorescence,[7] and Raman[6,8] spectroscopic techniques can be used to follow key species such as the uranyl ion where only the probe is within the radiation environment.[6] Fiber optics connect the probe to the electronics, allowing the radiation-sensitive components to be located at a distance from the harsh environment. The probes, made of metal and glass, can withstand significant radiation doses without failing.[8]

While the utility of Raman spectroscopy for detecting actinide species has been previously investigated,[9−11] this work explores applications within significantly more complex solutions. Namely, the ability to quantify the uranyl ion in solutions exhibiting variable nitric acid (HNO_3) and hydrofluoric acid (HF) concentration is demonstrated. In these systems, competing ligands create highly complex speciation behavior and, consequently, highly nonlinear optical response. To overcome this challenge, chemometric models are leveraged to build regression algorithms for high-fidelity quantification.

Optical monitoring and multivariate analysis provide insights into the fundamental chemistry of these multiligand systems. Specifically, the chemical speciation of the uranyl ion within solutions of variable HNO_3 and variable HF can be quantified using multivariate analysis. Two independent, multivariate methods for calculating the speciation of UO_2^{2+} are leveraged and compared. The methods are HypSpec2014 and multivariate curve resolution (MCR), where the mathematics differ

Received: August 14, 2023
Accepted: October 9, 2023
Published: October 27, 2023

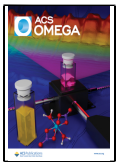

in such a way as to allow for a multiangled exploration of speciation. These techniques were used to determine the number of uranium species in solution. For a more comprehensive understanding and comparison, UV−vis absorbance data was also leveraged as a part of this study.

The findings from the speciation studies were used to inform and optimize subsequent chemometric regression models for quantification, e.g., to select the number of latent variables (model components) needed for partial least-squares-locally weighted regression (PLS-LWR) modeling, which quantifies the concentration of uranium in solution. PLS-LWR models were also used to measure the HNO_3 concentration. As a demonstration of how powerful the multivariate approach can be, models were also built to quantify HF based on the indirect effects on the Raman band structure.

Also included is a comparison of optical data from Raman and visible absorbance systems. While absorbance systems are more typically used to explore the electronic differences between chemical species, Raman is the more selective tool for UO_2^{2+} quantification. Comparing speciation impacts between the two optical approaches and the two mathematical analyses provides valuable insights into both the chemical behavior of the system and the robust quantification models needed to enable online monitoring.

EXPERIMENTAL SECTION

Materials. All chemicals were used without further purification: uranyl nitrate hexahydrate $[UO_2(NO_3)_2(H_2O)_6$, Spectrum, 98.0−102.0%], nitric acid (HNO_3, Sigma-Aldrich, 70% concentrated), and hydrofluoric acid (HF, Sigma, 48% concentrated).

In order to span a wide concentration range while limiting the number of samples and reducing the radioactive waste generated, a series of titrations were performed for a majority of the samples. One- and two-component solutions of UO_2^{2+}, HF, and HNO_3 were measured along with titrations of 1 or 2 M UO_2^{2+} with HF at various starting concentrations of HNO_3. With this method, the spectral fingerprints of the individual components, as well as any spectral interferences or chemical interactions, can be captured. The overall concentration ranges of each analyte are included in Table 1. There were a total of 331 unique samples measured. Due to the complexity of performing work within a contamination area (CA) fume hood, experiments were performed at ambient laboratory temperature conditions (~20 °C) and would be considered isothermal.

Table 1. Analyte Concentration Ranges Prepared for the Training and Validation Set Samples

analyte	concentration range (M)
UO_2^{2+}	0.43−2.0
HNO_3	0.20−7.8
HF	0.25−3.5

Instrumentation. The Raman and visible absorbance spectrometers used in this work were acquired from Spectra Solutions Inc. and consisted of high throughput volume phase holographic gratings with thermoelectrically cooled charge-coupled device (CCD)-based detectors. The Raman system employed a miniature fiber optic probe with a backscattering (180°) optical design and a continuous wave (CW) 250 mW, 671 nm excitation laser. The detector had an ~ 5 cm^{-1} resolution and an operating range of ~ 185−4495 cm^{-1}. A 1 s integration time was used for each measurement. The visible detector range was 395−874 nm, and an SLS205 Xenon arc lamp was purchased from ThorLabs Inc. (Newton, NJ). A 0.12 s integration time was used.

The cell holder pictured in Figure 1 contained fiber optic ports for the excitation and collection fibers of the visible spectrometer. These fibers are perpendicular to the Raman probe, allowing for the simultaneous interrogation of samples within a cuvette. All samples were measured in a 1 cm quartz cuvette. Although HF solutions can dissolve quartz, each sample was measured as quickly as possible, and no evidence was observed of damage to the cuvette. Water spectra were also collected periodically to check whether the signal remained consistent. For each sample, 100 spectra were collected for both Raman and visible absorbance measurements. Each sample was measured in replicates of 10 spectra and averaged.

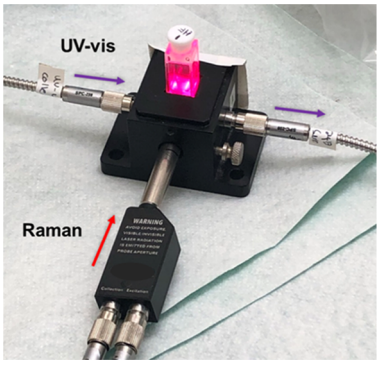

Figure 1. Cuvette holder showing the 671 nm Raman probe and the attached visible absorbance fiber optic cables.

Data Analysis via HypSpec. Formation constants (β) for the $UO_2F_n^{2-n+}$ complexes were determined from the visible absorbance and Raman spectra using HypSpec2014.[12] The absorbance spectra had all wavelengths below 481.5 and above 650 nm removed to eliminate portions of the spectra with excessive absorption or which contained only baseline and scattered light from the Raman laser, respectively. Raman spectra were first normalized to the area under the water band from approximately 2500−4000 cm^{-1}. Normalizing to the water band helps account for laser power fluctuations, and while pH can affect the shape of the water band, it has been found that, in general, the area under the curve does not vary significantly with pH changes.[13] Subsequently, portions of the Raman spectra below 500 cm^{-1} or above 2350 cm^{-1} were removed to eliminate the excess baseline and the large water band. Spectra of samples in which solids precipitated during titration were excluded from this analysis.

The UO_2^{2+} and F^- system forms three complexes, with formation constants denoted as β_1, β_2, and β_3, defined in eqs 1−3, respectively. Protonation of F^- was accounted for when fitting these values in HypSpec2014 by including both F^- and HF as species in the model with a pK_a of 3.17.[14]

$$\beta_1 = \frac{[UO_2F^+]}{[UO_2^{2+}][F^-]} \quad (1)$$

$$\beta_2 = \frac{[UO_2F_2(aq)]}{[UO_2^{2+}][F^-]^2} \quad (2)$$

https://doi.org/10.1021/acsomega.3c06007
ACS Omega 2023, 8, 41696−41707

$$\beta_3 = \frac{[UO_2F_3^-]}{[UO_2^{2+}][F^-]^3} \quad (3)$$

The formation constants were fit with models accounting for the formation of the NO_3^- complexes, $UO_2(NO_3)_n^{2-n+}$, and models that did not account for these complexes. From the available data set, the formation constants for the NO_3^- complexes were unable to be resolved, so the formation constants determined by Houwer and Görller-Walrand[15] were used. The inclusion of these complexes in the models resulted in slightly poorer fits with higher uncertainties; therefore, all results contained here ignore the existence of $UO_2(NO_3)_n^{2-n+}$ complexes.

Chemometric Modeling. MCR and PLS-LWR models were generated using MATLAB (R2022B) with the Eigenvector Research PLS-Toolbox (version 9.0). The same normalization step was done on the Raman data for MCR that was done for HypSpec. Further details on sample selection and additional preprocessing steps are outlined in the corresponding section of Results and Discussion.

RESULTS AND DISCUSSION

Uranyl Optical Fingerprint. The uranyl ion fingerprint is well characterized in the literature for a range of optical techniques.[16−19] In the case of Raman spectroscopy, for UO_2^{2+}, a primary response band is anticipated at ∼870 cm^{-1} that corresponds to the O ═ U ═ O ν_1 symmetric stretching frequency, which has been shown to be insensitive to the weakly complexing NO_3^- in HNO_3 solutions.[18] Both HNO_3 and UO_2^{2+} produce minor bands, which become visible at higher concentrations, and both impact the profile of the primary water band at 3300 cm^{-1}. Figure 2 presents an example of the spectral fingerprints of uranyl nitrate in 0 M HNO_3. The full Raman spectral response is shown in Figure 2A, with the UO_2^{2+} band shown in the inset. Also presented in Figure 2B is a simple calibration curve for the quantification of UO_2^{2+} in 0 M HNO_3 via Raman spectroscopy. Limits of detection (LOD) were calculated via the following equation:

$$\mathrm{LOD} = \frac{3s}{m} \quad (4)$$

where s is the standard deviation of the blank (water) and m is the slope of the calibration curve.[20]

The visible absorption spectrum is also well characterized and can be seen in Figure 2C. This fingerprint corresponds well to what has been previously reported in the literature.[10,21] The presence of additional complexing species such as HNO_3 can impact fingerprints, as discussed in subsequent sections. Figure 2D shows the calibration curve of UO_2^{2+} in 0 M HNO_3 for the absorbance spectra shown in Figure 2C.

Optical Impacts of Variable HNO_3. In the presence of increasing HNO_3, UO_2^{2+} speciation will change to include $UO_2NO_3^+$, $UO_2(NO_3)_2$, and $UO_2(NO_3)_3^-$.[15,22] Generally, these types of speciation changes are more easily followed via electronic spectroscopy such as UV−vis absorbance. Impacts to Raman can be observed but typically are more noticeable when switching between complexing ligands, as will be discussed in subsequent sections. This can be observed in Figure 3A,B, respectively. In Figure 3A, the Raman uranyl band at 873 cm^{-1} is stable across the range of HNO_3 concentrations up to 5.7 M. The visible absorbance bands, however, shift and change intensity with variations in the HNO_3 concentration (Figure 3B). Note, because the detector used here is unable to probe into the UV, only a limited portion of the UO_2^{2+} shoulder is observable in Figure 3B. The LOD calculations performed for uranyl ion in each HNO_3 concentration, shown in Table S1 in the Supporting Information, demonstrate the effects of band shifting. With an increase in initial HNO_3 concentration, the location of the Raman band did not change outside of the detector's resolution, and the LODs for uranyl ion remained relatively constant at about 1.5 mM. The visible absorption band chosen for quantification, however, shifted slightly from 488 to 483 nm, and there was a slight increase in the LODs from about 3 to 15 mM. This is also shown in Figure 3B, where the visible band at 488 nm decreases in

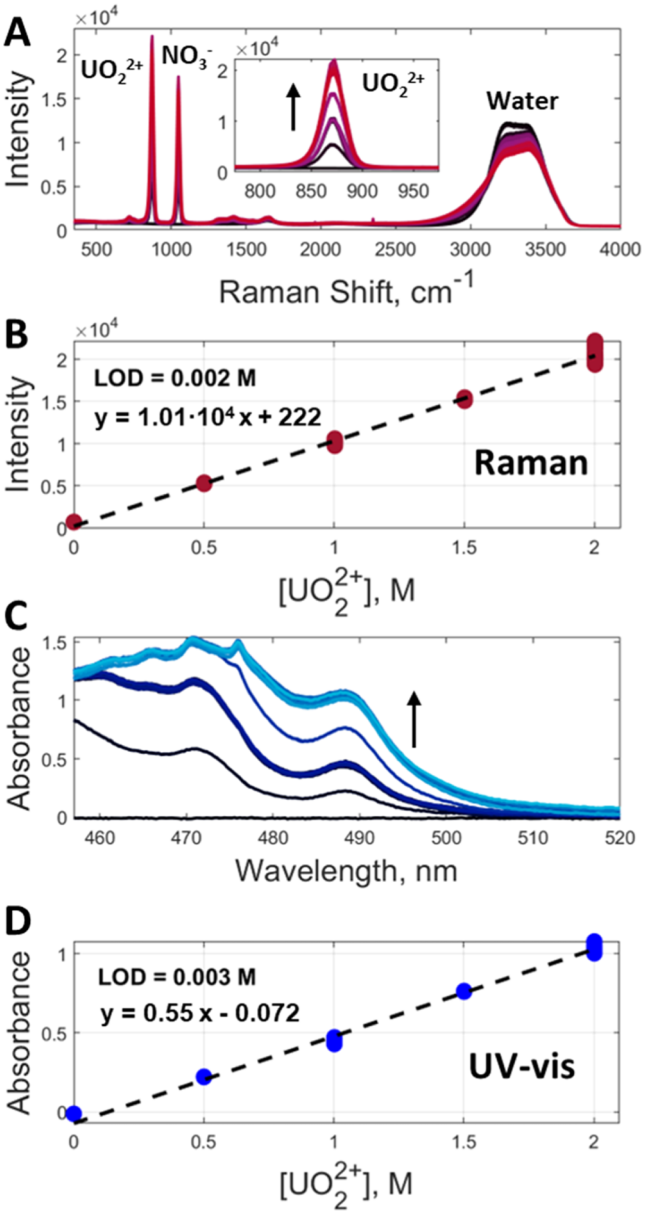

Figure 2. (A) Full Raman spectrum of 0.0−2.0 M uranyl nitrate in 0.0 M HNO_3. (B) Calibration curve of Raman intensity at 873 cm^{-1}, as a function of uranyl concentration, and calculated limit of detection (LOD). (C) Visible absorption spectrum of 0.0−2.0 M uranyl nitrate in 0.0 M HNO_3. (D) Calibration curve of visible absorbance at 488 nm, as a function of uranyl concentration, and calculated LOD. The arrows in parts A and C indicate the band increase due to an increase in uranium concentration.

https://doi.org/10.1021/acsomega.3c06007
ACS Omega 2023, 8, 41696−41707

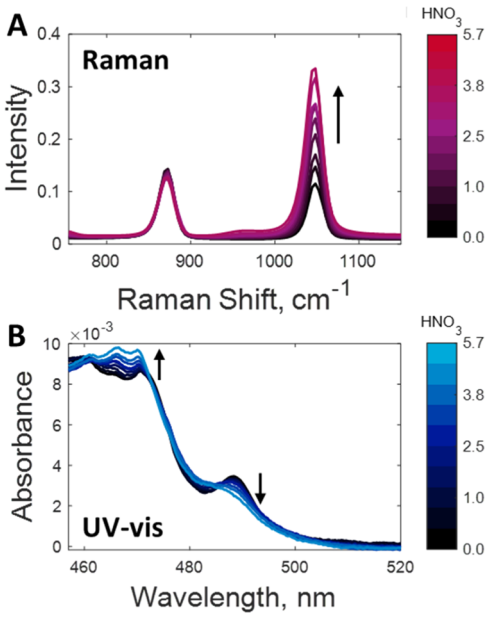

Figure 3. 1.0 M uranyl nitrate titrated with 0.0−5.7 M HNO_3 showing (A) Raman spectra and (B) visible absorbance spectra. The Raman spectra are shown normalized to the area under the uranyl band from 825 to 900 cm^{-1} to account for dilution and highlight changes in the nitrate band, and the visible absorbance spectra are normalized to the area under the curve from 450 to 525 nm to counteract the absorbance changes due to dilution.

intensity and shifts to a lower wavelength with an increase in HNO_3 concentration.

From the standpoint of characterizing uranyl ions within a process, there are several notable differences in the efficacy of these spectroscopic methods. For example, if the goal is to identify uranium ion speciation, a UV−vis approach is ideal, as detection of the uranyl ion in the UV region can be quite sensitive. However, if the goal is to quantify total UO_2^{2+} within a process with variable HNO_3, Raman spectroscopy enables more simplistic calibration curves because the shape and frequency of the Raman response band are more stable than that of UV−vis response of similar solution chemistries. These quantification approaches have been discussed elsewhere.[10,23,24]

UO_2^{2+} Fingerprint Impacts with HF. Quantifying the uranyl ion concentration becomes substantially more challenging when looking at chemical systems exhibiting multiple potential ligands to UO_2^{2+}. A key example is a uranyl system including both HNO_3 and HF. This can be a common situation in nuclear materials processing, where HF is added to prevent third phase formation and other process upsets.[25,26]

Figure 4 shows the impacts of increasing HF concentration on both the Raman and visible absorbance spectrum in the presence of different base HNO_3 concentrations. For this work, solutions of 1.0 and 2.0 M UO_2^{2+} were titrated with HF in 0−5.7 M HNO_3. For comparison, results are plotted for a subset of this data. Figure 4A−C shows the Raman spectra normalized to the area under the nitrate band from 980 to 1100 cm^{-1} to account for dilution and laser fluctuations and to visualize the change in the uranyl band. The uranyl Raman band shifts to a lower wavenumber, broadens, and decreases in intensity with increasing concentration of HF. The absorbance bands change shape notably across both variable HF and HNO_3, as seen in Figures 3B and 4D−F. Increasing optical complexity limits the accuracy of simple calibration curves, which must be calculated for each acid concentration, thereby requiring *a priori* knowledge of acid concentration in new samples in order to select the appropriate calibration curve against which to measure the sample. Advanced, nonlinear methods of analysis can provide high-fidelity analysis of uranyl ion in solutions of various acid/ligand compositions.

Speciation of UO_2^{2+} with HF. It is of interest to explore the complex speciation of this multicomponent system. Two

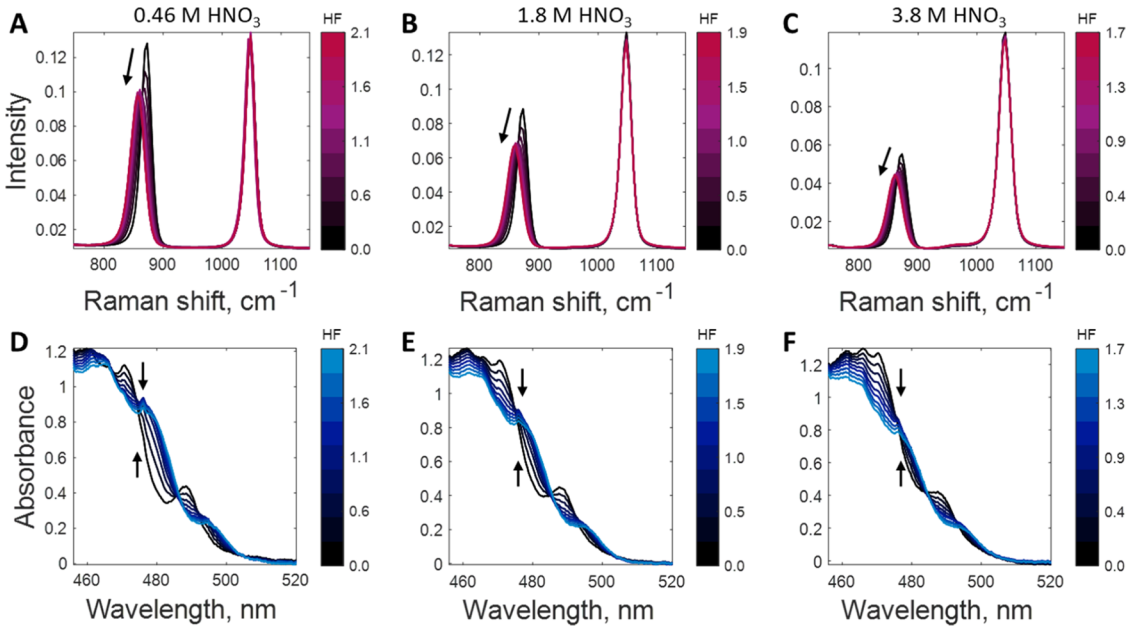

Figure 4. (A−C) Raman spectra and (D−F) visible absorbance spectra of 1.0 M uranyl titrated with up to 2.1 M HF in A, D: 0.46 M HNO_3; B, E: 1.8 M HNO_3; and C, F: 3.8 M HNO_3. The Raman spectra are shown normalized to the area under the nitrate band from 980 to 1100 cm^{-1}. The arrows indicate the spectral band shift corresponding to an increase in HF concentration.

https://doi.org/10.1021/acsomega.3c06007
ACS Omega 2023, 8, 41696−41707

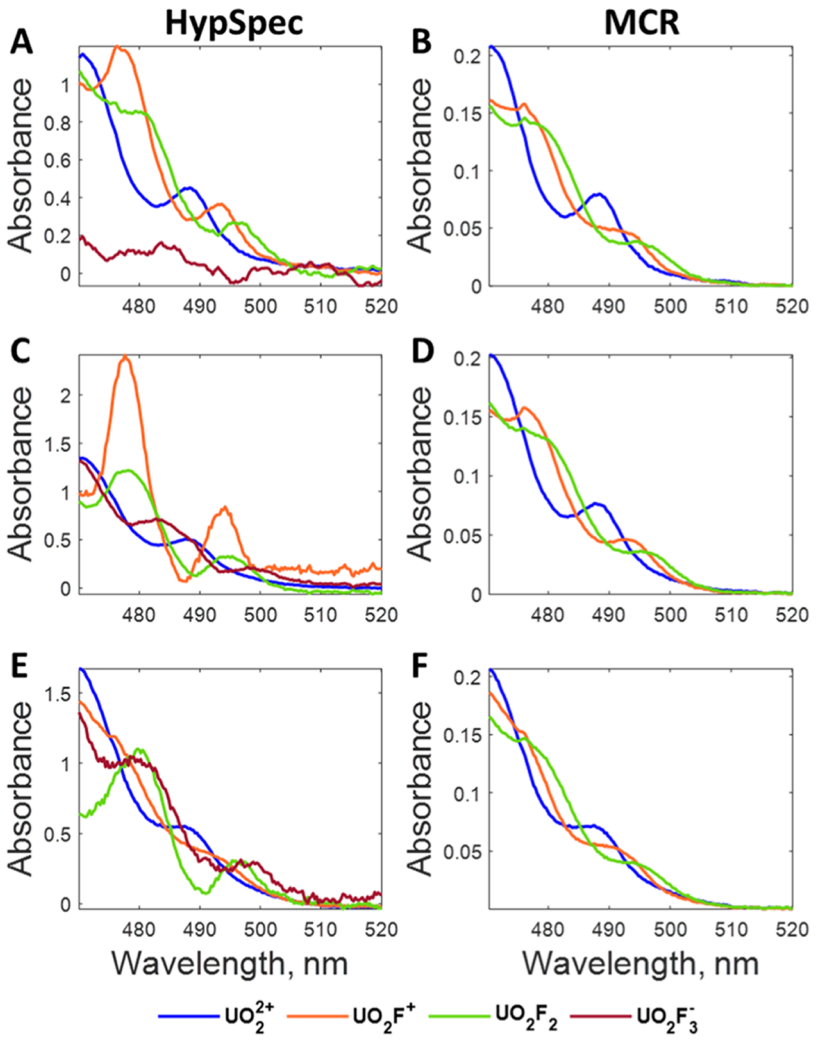

Figure 5. Comparison between HypSpec (left column) and MCR (right column) results fitting 4 components for HypSpec and 3 components for MCR for visible absorbance spectra of 1.0 M UO_2^{2+} titrated with 0.0−2.1 M HF in (A, B): 0.46 M HNO_3; (C, D): 1.8 M HNO_3; and (E, F): 3.8 M HNO_3.

tools were utilized for the spectral analysis: HypSpec and MCR via PLS-Toolbox. Data are partitioned, preprocessed, and decomposed differently within the two analyses.

Both methods were applied to the Raman and visible absorbance data sets to enable a comparison of spectral impacts of solution composition within each technique. Because quantification of uranyl ion within variable HNO_3 is well documented,[15,22,27] it does not represent a novel challenge for speciation characterization. Instead, efforts were focused on exploring speciation under variable HF concentrations within relatively constant HNO_3 matrices.

The deconvoluted signatures of fluoride species in visible absorbance analysis can be seen in Figure 5 for three concentrations of HNO_3 (0.46, 1.8, and 3.8 M) with titrated HF; the corresponding spectra are shown in Figure 4D−F. From the absorbance spectra, HypSpec identified four species, while MCR demonstrated the best fit with three species. The differing species in this case is $UO_2F_3^-$, though the presence of this particular species is minimal. The band locations and shapes agree well between the two mathematical approaches for the first three species, though relative intensities vary notably. For MCR, fitting a fourth species resulted in more noise and overlapping species peaks, which are indicators of overfitting. Figure S1 shows the MCR results when the fit was with four species. One limitation of MCR is rotational ambiguity, where the model can output more than one solution that can reproduce the original spectra.[28,29] This can be suppressed with the addition of constraints. In this case, the only constraint on the model was limiting the number of components, but the similarity between the results from HypSpec and MCR provides support that the MCR results are representative of the actual component spectra.

The HypSpec species fraction results and MCR scores from visible absorbance spectra are shown in Figure 6. These results are again shown fitting 4 species with HypSpec and 3 components in MCR. In Figure 6B,F, there is a slight increase in the scores for the UO_2^{2+} species at high F^- concentration, which could suggest the presence of a fourth species. The results showing the MCR fit with 4 components are shown in Figure S2. In Figure S2B, the MCR results fit a fourth species ($UO_2F_3^-$) at 0 M F^-, which is not possible. There was also more scatter in the replicate points in Figure S2F compared to Figure 6F, which only fit 3 species. Therefore, the best MCR results fit 3 species. Both techniques show speciation changes across each titration with HF, with speciation varying among the titrations due to the ratio of HNO_3 to HF. The results of

https://doi.org/10.1021/acsomega.3c06007
ACS Omega 2023, 8, 41696−41707

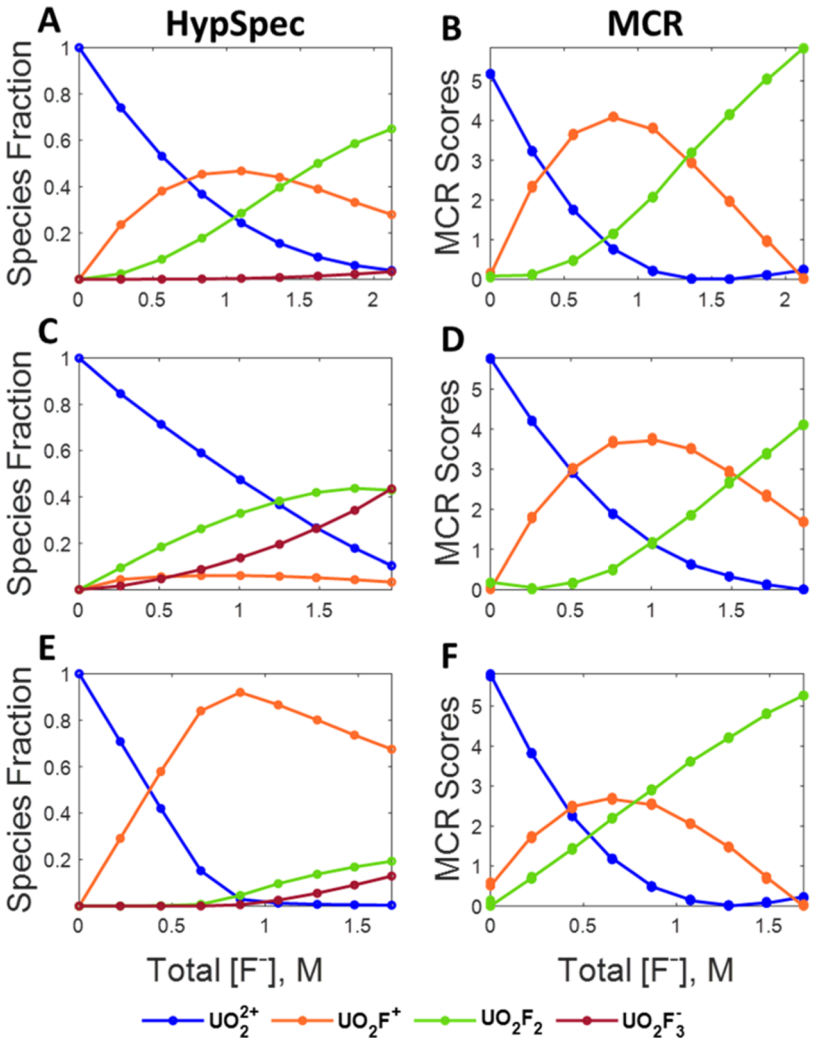

Figure 6. Speciation comparison between HypSpec (left column) and MCR (right column) results fitting 4 components for HypSpec and 3 components for MCR for visible absorbance spectra of 1.0 M UO_2^{2+} titrated with 0.0−2.1 M HF in (A, B): 0.46 M HNO_3; (C, D): 1.8 M HNO_3; and (E, F): 3.8 M HNO_3.

Table 2. Formation Constants for UO_2^{2+} with F^- Determined by Visible Absorbance Spectroscopy

	1.0 M UO_2^{2+}			2.0 M UO_2^{2+}		
initial [HNO_3] (M)	$\log\beta_1$	$\log\beta_2$	$\log\beta_3$	$\log\beta_1$	$\log\beta_2$	$\log\beta_3$
0.46	4.56 ± 0.01	8.62 ± 0.03	11.0 ± 0.3	4.611 ± 0.009	8.42 ± 0.05	12.54 ± 0.03
0.96	4.7 ± 0.1	10.38 ± 0.09	13.0 ± 0.5	5.56 ± 0.01	9.82 ± 0.03	[b]
1.80	4.1 ± 0.2	9.88 ± 0.03	14.5[a]	6.16 ± 0.01	11.56 ± 0.03	[b]
2.50	4.1 ± 0.4	10.88 ± 0.09	14.5 ± 0.2	5.42 ± 0.01	10.98 ± 0.02	[b]
3.18	4.26 ± 0.08	11.06 ± 0.03	13.9 ± 0.1	6.39 ± 0.02	9.82 ± 0.08	[b]
3.80	6.30 ± 0.05	9.8 ± 0.3	13.67 ± 0.04	6.82 ± 0.06	10.4 ± 0.2	[b]
4.82	6.7 ± 0.1	10.9 ± 0.4	12 ± 3	7.92 ± 0.02	13.39 ± 0.05	[b]
5.70	5.9 ± 0.2	8 ± 4	15 ± 1	7.75 ± 0.02	13.1 ± 0.04	[b]

[a]Uncertainty unable to be determined [b]β_3 unable to be fit

both modeling techniques show a decrease in the uncomplexed UO_2^{2+} at low HF concentrations and increasing amounts of the higher-order fluoride species forming at higher concentrations of HF. While the amounts of each species vary depending on the analysis method, the locations of the maximal species fractions are similar. In comparing these two analysis techniques, it is worth noting the difference in the *y*-axis scale. For HypSpec, the data output is in species fraction where the totals of each species sum to 1. For MCR, the scores are calculated differently, resulting in a somewhat arbitrary *y*-axis scale, but the relative amounts of each species are comparable to HypSpec.

Mathematics for determining formation constants via the HypSpec approach is described in the Experimental Section. The formation constants of the uranyl fluoride species show notable variation with the initial concentration of HNO_3. For the UO_2F^+ and UO_2F_2(aq) complexes, the formation constants increase with the HNO_3 concentration, as shown in Table 2.

https://doi.org/10.1021/acsomega.3c06007
ACS Omega 2023, 8, 41696−41707

This can also be seen in the 1.8 M HNO_3 spectra in Figure 6C, where the species fraction of $UO_2F_3^-$ appears to be greater than that in Figure 6A,E, though this trend is difficult to discern due to the greater uncertainty in the formation constants for those measurements. At lower initial HNO_3 concentrations, the formation constants are comparable to those published by Grenthe et al.[30] and Tian and Rao[31] despite the lack of correction for ionic strength here.

The Raman spectra were fit with HypSpec using an approach similar to that of the visible absorbance data. This gave $\beta_1 = 6.82 \pm 0.07$ and $\beta_2 = 9.57 \pm 0.04$. No value for β_3 could be fit from the Raman spectra. This can be attributed to the limited formation of the $UO_2F_3^-$ complex and lower Raman sensitivity compared with the visible spectra for this analyte. Extending the titration to capture spectra with a higher $[F^-]/[UO_2^{2+}]$ ratio has been observed to yield both the $UO_2F_3^-$ and $UO_2F_4^{2-}$ complexes.[27]

The Raman results are presented in Figure 7. In both HypSpec and MCR analyses, three species were distinguishable from the Raman data. A fourth species, such as the $UO_2F_3^-$ complex observed by UV−vis, was not observed, but the lack of this species may contribute to the physically unreasonable negative intensity seen in the UO_2F_2 spectra in Figure 7A. Using HypSpec, analysis of Raman data proved difficult, as the software could not distinguish between UO_2^{2+} and HNO_3 spectra if input as a set containing only one HNO_3 concentration. To combat this, data were partitioned into separate sets for each starting UO_2^{2+} concentration, with multiple HNO_3 matrices, into which HF was titrated. Each set was then fit using HypSpec.

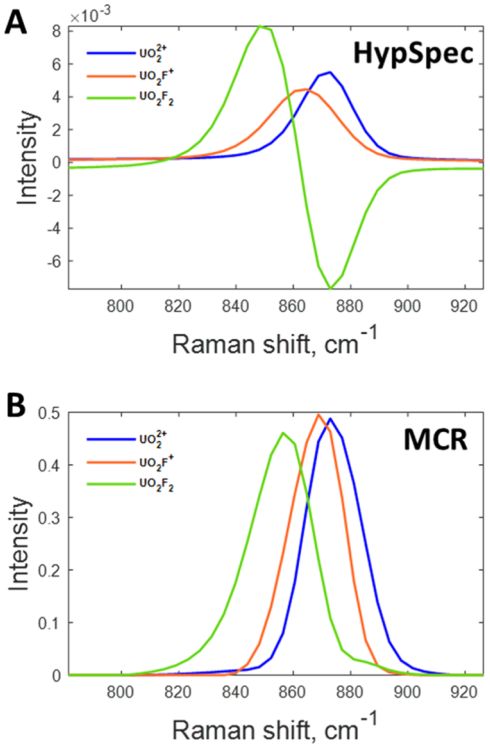

Figure 7. HypSpec (A) and MCR (B) components from fitting Raman spectra with 3 components.

For a direct comparison to the HypSpec data presented in Figure 7, the same data sets were also selected for analysis by MCR. MCR models of Raman spectra were tested, fitting both 3 and 4 components. The results fitting 4 components are shown in Figure S3. In this figure, while the MCR model was able to fit a fourth component, it appears to have a similar character as the first component and therefore appears to be an overfit of the data. Thus, 3 components were chosen as the appropriate fit of the data and are shown in Figure 7B. MCR components show a behavior similar to that of the HypSpec results, with a shift in the UO_2^{2+} Raman band to lower wavenumbers with the formation of higher-order fluoride complexes.

The results of both the HypSpec and MCR data fits are also in agreement with the literature. Nguyen-Trung et al. have collected Raman spectra of samples with a broader range of $[F^-]/[UO_2^{2+}]$ ratios and were able to observe these complexes.[27] They observed a consistent decrease of 12 cm^{-1} in the Raman ν_1 band for each additional F^- added to UO_2^{2+}. Table 3 contains the peak locations for the complexes determined in this work using HypSpec and MCR, as well as those published by Nguyen-Trung.[27] While there is close agreement in the Raman bands of the UO_2^{2+} and $UO_2F_2(aq)$ complexes, the UO_2F^+ complex, while still between UO_2^{2+} and $UO_2F_2(aq)$, is not in such close agreement. Despite this, there is the same overall trend of a shift in peak location with the formation of higher-order fluoride complexes.

Table 3. Location of the Raman O═U═O ν_1 Band, in cm^{-1}, for UO_2^{2+} and $UO_2F_n^{2-n+}$ Complexes

complex	this work, HypSpec	this work, MCR	Nguyen-Trung et al.[27]
UO_2^{2+}	873	873	870
UO_2F^+	865	869	858
$UO_2F_2(aq)$	848	856	846
$UO_2F_3^-$			834
$UO_2F_4^{2-}$			822

Quantification of UO_2^{2+}, HNO_3, and HF. Previous sections provide key insight into the complexity of optical signals from a system, including uranyl ions (UO_2^{2+}), HNO_3, and HF. In a process where the goal would be to quantify these chemical targets in situ and in real time, data processing must move beyond univariate analysis in order to deal with nonlinearity of signal due to interactions between chemical species in solution. Here, multivariate analysis is necessary to accurately characterize and quantify the analytes. Specifically, multivariate regression approaches that can be flexible to nonlinearity are ideal. Regression was performed using Raman spectra due to the lack of visible absorbance of HNO_3 and HF and the low absorbance of uranyl species in the wavelength region utilized in this study.

The Raman spectral data, shown in Figures 2−4, were used to construct regression models that quantitatively measure the analytes of interest. Application of the principal component regression (PCR) and partial least-squares (PLS) methods to the spectral matrices to develop quantitative predictive models utilized the spectral data with corresponding concentration data for each of the analyte components: uranyl nitrate, HNO_3, and HF. The spectra were partitioned into a calibration (training) set used to build the models and a validation set, which was unseen by the algorithm during calibration and was measured using the calibrated algorithm.

Prior to performing regression methods, the data were conditioned using several preprocessing steps. To account for

https://doi.org/10.1021/acsomega.3c06007
ACS Omega 2023, 8, 41696−41707

Table 4. Variables Used in Chemometric Analysis of the Raman Spectra of Samples Containing $UO_2(NO_3)_2$, HNO_3, and/or HF, with Model Performance Statistics and Metrics[a]

analyte	modeling method and preprocessing	RMSEC	RMSECV	RMSEP	R^2 (calcd)
UO_2^{2+}	PLS-LWR (locally weighted regression) 1000 local points baseline, OH-normalization, first derivative, MC	0.01331	0.02486	0.04124	0.9996
HNO_3	PLS-LWR (locally weighted regression) 125 local points baseline, OH-normalization, first derivative, MC	0.03816	0.1726	0.3079	0.9996
HF	PLS-LWR (locally weighted regression) 500 local points baseline, OH-normalization, first derivative, MC	0.05265	0.08061	0.8031	0.9935

[a]For all models, the wavenumber range included was 340−4500 cm^{-1}; three latent variables were used; and the total number of samples in the training set was 4119.

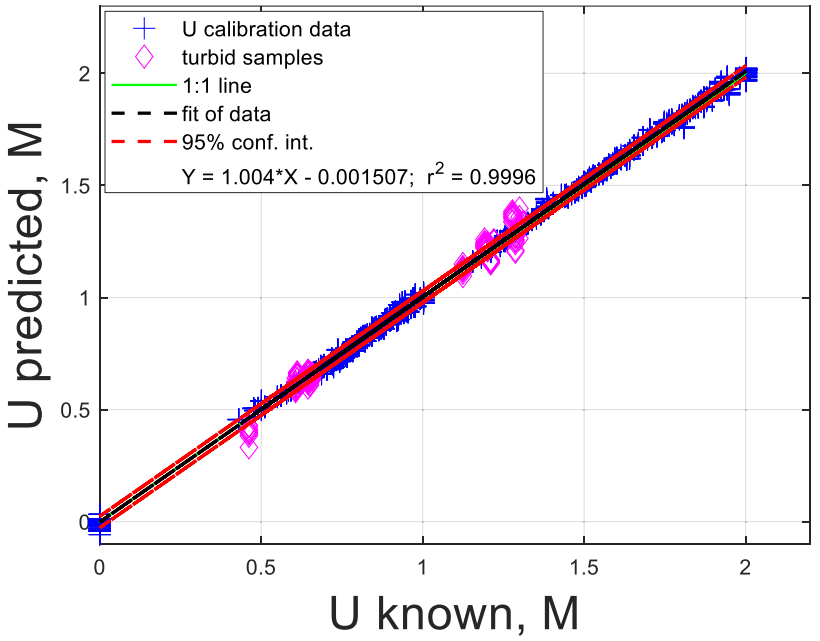

Figure 8. PLS-LWR results of a model for uranyl concentration, showing predicted vs known concentrations under variable nitric and hydrofluoric acid.

fluctuations in laser power, light scattering due to turbidity, and for baseline drift/nonlinearity due to sample fluorescence, Raman spectra were normalized to the area of the water band (2700−3700 cm^{-1}). This was followed by a first derivative (second-order polynomial, using a 15-point filter width) to correct the baseline and minimize the effects of background dissimilarities between the calibration and validation sets. The final step was applying mean centering to the data to ensure equal weightings of the high and low concentrations. Cross-validation was performed using a "custom set" removal technique, where each unique sample represented by 10 replicate measured spectra was removed. The remaining samples were then used to form a model that was then applied to the removed sample. This process is repeated until all unique samples (with their replicates) have been removed in turn. Further details of modeling parameters are listed in Table 4.

The PLS and PCR methods have been used extensively in the field of chemistry, including modeling of spectroscopic data, as detailed elsewhere.[32−34] The PCR and PLS methods were both evaluated using the PLS-Toolbox.[35]

Table 4 lists the model statistics for the PLS analyses. These include the root-mean-square error of calibration (RMSEC), which is a measure of the potential to use this model to predict the concentrations in the training set used for the calibration, the root-mean-square error of cross-validation (RMSECV), which measures the model's ability to predict samples left out of the calibration set, and the root-mean-square error of prediction (RMSEP), which is a measure of the error of the validation set. These values can be interpreted as ± concentration error.[36] The PLS analysis utilized the SIMPLS algorithm (statistically inspired modification of PLS).[37] A variation on the PLS modeling, using a locally weighted regression (LWR) to accommodate nonlinear physical systems, was added to the analysis. The LWR method breaks the training set into smaller, nearly linear segments and calibrates the PLS regression over these smaller training ranges. LWR is useful for the analytes in this study because the analyte−analyte interactions introduce subtle changes in the Raman spectra via metal−ligand influences and changes in ionic strength. LWR models were optimized by a survey method that first selected the number of local points used for the model based on approximately one-half of the total number of spectra

https://doi.org/10.1021/acsomega.3c06007
ACS Omega 2023, 8, 41696−41707

comprising the calibration set, with 2000 local points initially chosen. This was followed by running the analysis again with one-quarter (1000), one-eighth (500), and so on. Results for these analyses were compared, and the number of local points chosen corresponded to the optimal RMSEC, RMSECV, and RMSEP values. The number of local points and the number of training samples for each model are listed in Table 4.

The PLS-LWR regression results for the UO_2^{2+} model are shown in Figure 8 in the form of a parity plot of the predicted vs known concentrations of uranyl ion under variable HNO_3 and HF concentrations. This figure shows the calibration data (training set) as blue "+" symbols, with the validation data (separate from the calibration set) as magenta-diamond symbols. The validation samples were a set of samples that showed variable amounts of turbidity and, in general, would be expected to show a higher variation in the prediction of concentration. The turbid samples were identified by eye and confirmed by observing an increase in baseline absorbance signal, indicative of solid particles blocking the light path. In this case, while the error of prediction for the validation data (RMSEP) is approximately 4 times higher than the RMSEC value, it is only twice the value of the RMSECV. Despite the larger values for the RMSEP and RMSECV, the overall magnitude of the error is small relative to the total concentration range studied (RMSECV = 0.025 and RMSEP = 0.041 M compared to 2.0 M total uranyl ion). The RMSECV value represents approximately 1% uncertainty in the measurement, which is expected to be larger compared to the uncertainty in the known UO_2^{2+} concentration, which was 0.1%.

The ability to accurately measure UO_2^{2+} within highly turbid samples, as well as in the presence of variable HF and HNO_3, is an advancement in this technique. While previous studies have shown the quantitative measurement of uranium nitrate in the presence of variable nitrate and nitric acid concentrations,[6,13,32,38−41] this work demonstrates the first example where uranium is quantitatively measured in the presence of both variable nitric acid and hydrofluoric acid using Raman spectroscopic methods.

The PLS-LWR regression results for nitric acid (HNO_3) are contained in the parity plots shown in Figure S4, with the model statistics and variables used shown in Table 4. The prediction of nitric acid shows excellent agreement with expected values for both the calibration data and for the validation data set. The errors associated with the HNO_3 are excellent (RMSECV = 0.17 M), when compared to the total range of concentration measured (0−8 M). This equates to approximately 2% uncertainty, which is greater than the uncertainty in the known HNO_3 concentration, which was approximately 0.3%. The predictions of turbid samples (Table 4) are approximately twice the value of the RMSECV values, which is consistent with the uranyl nitrate system.

The PLS-LWR results for the HF predictions are detailed in Table 4 and are shown in the parity plot in Figure S5. The calibration data are evenly distributed along the 1:1 line with a reasonable r^2 value (0.9935). In addition, the RMSECV value (0.08 M) is less than a factor of 2 higher than the RMSEC (0.05 M), indicating the robustness of the model. The RMSECV represents 2% of the total HF concentration studied (3.5 M) compared to 0.3% uncertainty in the known HF concentrations. The dissociated F^- ion does not have a unique Raman signal, and HF does not exhibit a strong signal under these conditions, so the ability to quantify HF in solution based solely on the influence of HF on the other bands (primarily the uranyl band) is significant. The predictions for HF on the validation set, which consisted of turbid samples, differ dramatically from the uranyl nitrate and nitric acid systems, in that the model greatly underpredicts the concentrations for these samples. In this case, the RMSEP value indicates a divergent behavior for the validation set. The lower predicted concentrations for HF in these turbid samples indicate the formation of a precipitated solid containing a fluoride species, which depletes the concentration of HF in the solution phase. While the solvated fluoride concentration was not independently determined through a secondary method, the precipitate was observed in solutions in which HF, HNO_3, and uranyl nitrate were present at relatively high concentrations. With solids only forming at high fluoride concentrations, it is likely that the solid contains fluoride and possibly forms a uranyl complex with more than one fluoride. In such a case, the HF model would be more greatly affected by the loss of solution phase HF than the uranyl model with a greater dependence on the concentration of F^- compared to UO_2^{2+}, which could explain the larger RMSEP for HF than uranyl. The validation set contains solutions at higher ionic strengths than those contained in the calibration set. The speciation trends in lower ionic strength solutions vary from those in higher ionic strength solutions. This particularly impacts the speciation of fluoride, which has no strong primary band but is quantified by the effect it creates on the uranyl band. In nonturbid, lower ionic strength samples, which comprise the calibration set of data, speciation to higher-order uranyl fluorides (and shift of the uranyl band to lower wavenumbers) correlates to increases in HF concentration; this relationship does not hold for turbid samples, in which a fluoride species precipitates with increasing HF concentration. As such, the model of fluoride is highly dependent on the speciation profile with increasing HF concentration; this profile differs in the low and high ionic strength solutions.

The number of principal components (PC) considered useful to include in each model is related to the rank of the data set and is conveniently determined by viewing the magnitude of each successive eigenvalue as a function of principal components included. Plots of the eigenvalues vs number of PC's retained are shown in Figure S6 for both mean-centered (Figure S6A) and nonmean-centered (Figure S6B) data. The sharp decrease in the magnitude for the first two or three eigenvalues indicates that three or possibly four factors are present within the data set. The models for the three species, UO_2^{2+}, HNO_3, and HF, can be determined by three model components in both principal component analysis (PCA) and PLS. To interpret the performance of the PCA and PLS models, it is instructive to view the principal components and their respective scores.

The first three PCs (PC1, PC2, PC3) are plotted in Figure S7, showing the expanded region around 700−1300 cm^{-1}, which includes the primary UO_2^{2+} and NO_3^- bands. Note that a first derivative is applied in preprocessing; therefore, the PCs in Figure S7 appear as a first derivative of the normal Raman bands. The PC1 and PC2 in this figure show predominantly a linear combination of the primary UO_2^{2+} and NO_3^- bands centered at 873 and 1050 cm^{-1}, respectively. PC3 is predominantly composed of signal from the uranyl band, red-shifted approximately 20 cm^{-1}. Plotting the scores of these in a 3-dimensional plot shows the contributions along each of the first three PCs. The scores in the PC1-PC2 plane are

https://doi.org/10.1021/acsomega.3c06007
ACS Omega 2023, 8, 41696−41707

aligned in the order of increasing uranium concentration, as shown in Figure S8. Color-coding the plot instead by increasing HNO_3 concentrations, as shown in Figure S9, demonstrates that the scores increase again in the PC1-PC2 plane but in the cross diagonal (orthogonal) compared to the uranium trend. Plotting the same scores, color-coded with respect to increasing HF concentration, as shown in Figure S10, the alignment predominately directs down PC3. The first three PCs are heavily influenced by the contributions of the three primary analytes; the scores of PC1 and PC2 are jointly aligned with the uranyl ion and nitric acid on the PC cross diagonals, and the scores of PC3 are directly aligned with the concentrations of HF.

While this work is limited to focusing on the interaction and binding complexity of competing ligands (F^- vs NO_3^-) on uranyl ion, it should be noted that in complex nuclear fuel reprocessing solutions, other constituents, including transition and lanthanide metal fission products (FPs), will be present. It is expected that these will add complexity to the quantitative analysis, due to many known FPs being UV−vis and Raman active. By judicious inclusion to the chemometric training set of FP species known or expected to be present, the deleterious effect of these potentially interfering species can be mitigated. In our past work, the effect of added interferents simulating corrosion and fission products was studied.[42] The effect on model performance with added interfering components in solution that were not included within the training data set was tested, with satisfactory results. As expected, it was found that by including the interfering species within the training set, the quantitative determination of target analytes could be improved.[42]

CONCLUSIONS

The quantitative measurement of the uranyl ion concentration was studied in the presence of multiple complexing ligands within complex acid media. Using two optical spectroscopic techniques (Raman and visible absorbance spectroscopy), quantitative models based on partial least-squares-locally weighted regression (PLS-LWR) were developed to predict the concentration of UO_2^{2+} over the concentration range of 0.43−2.0 M (U), in the presence of varying amounts of nitric acid (0.20−7.8 M) and hydrofluoric acid (0.25−3.5 M). The variation in the Raman and absorbance spectral bands as a function of nitric acid and hydrofluoric acid was also used as a basis for the quantitative measurement of both HNO_3 and HF by using PLS-LWR regression models. The speciation changes of uranyl ions, with the addition of both nitrate and fluoride, were considered with respect to the changes in the optical spectral signatures based on the coordination sphere changes of uranium due to complexation. The formation constants, β_n, for the respective $UO_2F_n^{2-n+}$ complexes (where n = 1−3) were determined and showed dependence on nitric acid concentration. The speciation modeling with HypSpec suggested the presence of up to 4 uranyl fluoride components compared to the multiplicative curve resolution (MCR) method, which isolated 3 components. Overall, this work demonstrates the utility of optical-based online monitoring for both fundamental speciation and quantitative analysis, particularly when partnered with multivariate data analysis approaches.

ASSOCIATED CONTENT

Supporting Information

The Supporting Information is available free of charge at https://pubs.acs.org/doi/10.1021/acsomega.3c06007.

Table of Raman UO_2^{2+} peak locations as a function of HNO_3 concentration as well as figures with additional chemometric modeling results, including MCR results fitting 4 components and PLS-LWR results, including HNO_3 and HF parity plots, eigenvalue plots, and results of PCA analysis (PDF)

AUTHOR INFORMATION

Corresponding Authors

Samuel A. Bryan − *Energy and Environment directorate, Pacific Northwest National Laboratory, Richland, Washington 99352, United States;* orcid.org/0000-0002-8826-0880; Phone: 1 509 375 5648; Email: sam.bryan@pnnl.gov

Amanda M. Lines − *Energy and Environment directorate, Pacific Northwest National Laboratory, Richland, Washington 99352, United States*; Phone: 1 509 375 5689; Email: amanda.lines@pnnl.gov

Authors

Heather M. Felmy − *Energy and Environment directorate, Pacific Northwest National Laboratory, Richland, Washington 99352, United States;* orcid.org/0000-0002-2548-7690

Nathan P. Bessen − *Energy and Environment directorate, Pacific Northwest National Laboratory, Richland, Washington 99352, United States;* orcid.org/0000-0003-2980-6107

Hope E. Lackey − *Energy and Environment directorate, Pacific Northwest National Laboratory, Richland, Washington 99352, United States*

Complete contact information is available at: https://pubs.acs.org/10.1021/acsomega.3c06007

Notes

The authors declare no competing financial interest.

ACKNOWLEDGMENTS

This research was supported by the U.S. Department of Energy, Office of Nuclear Energy, through the Nuclear Technologies R&D Program and was performed at the Pacific Northwest National Laboratory (PNNL) operated by Battelle for the U.S. Department of Energy under Contract DE-AC05-76RL01830.

REFERENCES

(1) Sims, R. E. H. Renewable energy: a response to climate change. *Sol. Energy* **2004**, *76* (1), 9−17.

(2) Brook, B. W.; Alonso, A.; Meneley, D. A.; Misak, J.; Blees, T.; van Erp, J. B. Why nuclear energy is sustainable and has to be part of the energy mix. *Sustainable Mater. Technol.* **2014**, *1*−*2*, 8−16.

(3) Knapp, V.; Pevec, D. Promises and limitations of nuclear fission energy in combating climate change. *Energy Policy* **2018**, *120*, 94−99.

(4) Locatelli, G.; Mancini, M.; Todeschini, N. Generation IV nuclear reactors: Current status and future prospects. *Energy Policy* **2013**, *61*, 1503−1520.

(5) Poinssot, C.; Bourg, S.; Ouvrier, N.; Combernoux, N.; Rostaing, C.; Vargas-Gonzalez, M.; Bruno, J. Assessment of the environmental

footprint of nuclear energy systems. Comparison between closed and open fuel cycles. *Energy* **2014**, *69*, 199−211.
(6) Lines, A. M.; Hall, G. B.; Sinkov, S.; Levitskaia, T.; Gallagher, N. B.; Lumetta, G. J.; Bryan, S. A. Overcoming Oxidation State-Dependent Spectral Interferences: Online Monitoring of U(VI) Reduction to U(IV) via Raman and UV−vis Spectroscopy. *Ind. Eng. Chem. Res.* **2020**, *59* (19), 8894−8901.
(7) Sadergaski, L. R.; Andrews, H. B. Simultaneous quantification of uranium(VI), samarium, nitric acid, and temperature with combined ensemble learning, laser fluorescence, and Raman scattering for real-time monitoring. *Analyst* **2022**, *147* (18), 4014−4025.
(8) Lines, A. M.; Tse, P.; Felmy, H. M.; Wilson, J. M.; Shafer, J.; Denslow, K. M.; Still, A. N.; King, C. K.; Bryan, S. A. On-line, real-time analysis of highly complex processing streams: Quantification of analytes in Hanford tank sample. *Ind. Eng. Chem. Res.* **2019**, *58* (47), 21194−21200.
(9) Bryan, S. A.; Levitskaia, T. G.; Johnsen, A. M.; Orton, C. R.; Peterson, J. M. Spectroscopic monitoring of spent nuclear fuel reprocessing streams: an evaluation of spent fuel solutions via Raman, visible, and near-infrared spectroscopy. *Radiochim. Acta* **2011**, *99* (9), 563−571.
(10) Lines, A. M.; Hall, G. B.; Sinkov, S. I.; Levitskaia, T.; Gallagher, N. B.; Lumetta, G. J.; Bryan, S. A. Overcoming oxidation state dependent spectral interferences: On-line monitoring of U(VI) reduction to U(IV) via Raman and UV−vis spectroscopy. *Ind. Eng. Chem. Res.* **2020**, *59*, 8894−8901.
(11) Lumetta, G. J.; Allred, J. R.; Bryan, S. A.; Hall, G. B.; Levitskaia, T. G.; Lines, A. M.; Sinkov, S. I. Simulant testing of a co-decontamination (CoDCon) flowsheet for a product with a controlled uranium-to-plutonium ratio. *Sep. Sci. Technol.* **2019**, *54* (12), 1977−1984.
(12) Gans, P.; Sabatini, A.; Vacca, A. Investigation of equilibria in solution. Determination of equilibrium constants with the HYPERQUAD suite of programs. *Talanta* **1996**, *43* (10), 1739−1753.
(13) Nelson, G. L.; Lines, A. M.; Casella, A. J.; Bello, J. M.; Bryan, S. A. Development and testing of a novel micro-Raman probe and application of calibration method for the quantitative analysis of microfluidic nitric acid streams. *Analyst* **2018**, *143* (5), 1188−1196.
(14) Harris, D. C. *Quantitative Chemical Analysis*, 8th ed.; Macmillan, 2010.
(15) De Houwer, S.; Görller-Walrand, C. Influence of complex formation on the electronic structure of uranyl. *J. Alloys Compd.* **2001**, *323*−*324*, 683−687.
(16) Vopálka, D.; Štamberg, K.; Motl, A.; Drtinová, B. The study of the speciation of uranyl−sulphate complexes by UV−Vis absorption spectra decomposition. *J. Radioanal. Nucl. Chem.* **2010**, *286* (3), 681−686.
(17) Maya, L.; Begun, G. M. A Raman-Spectroscopy Study of Hydroxo and Carbonato Species of the Uranyl(VI) Ion. *J. Inorg. Nucl. Chem.* **1981**, *43* (11), 2827−2832.
(18) Brooker, M. H.; Huang, C. B.; Sylwestrowicz, J. Raman spectroscopic studies of aqueous uranyl nitrate and perchlorate systems. *Journal of Inorganic and Nuclear Chemistry* **1980**, *42* (10), 1431−1440.
(19) Nguyen-Trung, C.; Palmer, D.; Begun, G. M.; Mesmer, R. E. Uv-Visible and Raman-Spectroscopic Studies of the Hydrolysis of the Uranyl(VI) Ion in Neutral and Basic Solutions at 25 °C, 0,1 MPa. *Chem. Geol.* **1988**, *70* (1−2), 190.
(20) Harris, D. C. *Quantitative Chemical Analysis*, 7th ed.; W.H. Freeman and Co.: New York, NY, 2007.
(21) Mckay, H. A. C.; Woodhead, J. L. Spectrophotometric Study of Nitrate Complexes of Uranium(IV). *J. Chem. Soc.* **1964**, 717.
(22) Ikeda-Ohno, A.; Hennig, C.; Tsushima, S.; Scheinost, A. C.; Bernhard, G.; Yaita, T. Speciation and Structural Study of U(IV) and -(VI) in Perchloric and Nitric Acid Solutions. *Inorg. Chem.* **2009**, *48* (15), 7201−7210.
(23) Nee, K.; Bryan, S. A.; Levitskaia, T. G.; Kuo, J. W. J.; Nilsson, M. Combinations of NIR, Raman spectroscopy and physicochemical measurements for improved monitoring of solvent extraction processes using hierarchical multivariate analysis models. *Anal. Chim. Acta* **2018**, *1006*, 10−21.
(24) Nelson, G. L.; Lines, A. M.; Bello, J. M.; Bryan, S. A. Online Monitoring of Solutions Within Microfluidic Chips: Simultaneous Raman and UV-Vis Absorption Spectroscopies. *ACS Sens.* **2019**, *4* (9), 2288−2295.
(25) Lumetta, G. J.; Swanson, J. L.; Barker, S. A. Process Chemistry for the Pretreatment of Hanford Tank Wastes. In *Chemical Pretreatment of Nuclear Waste for Disposal*, Schulz, W. W.; Horwitz, E. P., Eds.; Springer US: Boston, MA, 1994; pp 39−49.
(26) Lumetta, G. J.; Wagner, M. J.; Carlson, C. D. Actinide, strontium, and cesium removal from Hanford radioactive tank sludge. *Solvent Extr. Ion Exch.* **1996**, *14* (1), 35−60.
(27) Nguyen Trung, C.; Begun, G.; Palmer, D. A. Aqueous uranium complexes. 2. Raman spectroscopic study of the complex formation of the dioxouranium (VI) ion with a variety of inorganic and organic ligands. *Inorg. Chem.* **1992**, *31* (25), 5280−5287.
(28) Golshan, A.; Abdollahi, H.; Beyramysoltan, S.; Maeder, M.; Neymeyr, K.; Rajko, R.; Sawall, M.; Tauler, R. A review of recent methods for the determination of ranges of feasible solutions resulting from soft modelling analyses of multivariate data. *Anal. Chim. Acta* **2016**, *911*, 1−13.
(29) de Juan, A.; Jaumot, J.; Tauler, R. A. Multivariate Curve Resolution (MCR). Solving the mixture analysis problem. *Anal. Methods* **2014**, *6* (14), 4964−4976.
(30) Grenthe, I.; Fuger, J.; Konings, R. J.; Lemire, R. J.; Muller, A. B.; Nguyen-Trung, C.; Wanner, H. *Chemical Thermodynamics of Uranium*; Elsevier: Amsterdam, 1992; Vol. *1*.
(31) Tian, G.; Rao, L. Effect of Temperature on the Complexation of Uranium(VI) with Fluoride in Aqueous Solutions. *Inorg. Chem.* **2009**, *48* (14), 6748−6754.
(32) Nelson, G. L.; Asmussen, S. E.; Lines, A. M.; Casella, A. J.; Bottenus, D. R.; Clark, S. B.; Bryan, S. A. Micro-Raman Technology to Interrogate Two-Phase Extraction on a Microfluidic Device. *Anal. Chem.* **2018**, *90* (14), 8345−8353.
(33) Lackey, H. E.; Nelson, G. L.; Lines, A. M.; Bryan, S. A. Reimagining pH Measurement: Utilizing Raman Spectroscopy for Enhanced Accuracy in Phosphoric Acid Systems. *Anal. Chem.* **2020**, *92* (8), 5882−5889.
(34) Clifford, A. J.; Lackey, H. E.; Nelson, G. L.; Bryan, S. A.; Lines, A. M. Raman Spectroscopy Coupled with Chemometric Analysis for Speciation and Quantitative Analysis of Aqueous Phosphoric Acid Systems. *Anal. Chem.* **2021**, *93* (14), 5890−5896.
(35) Wise, B. M.; Gallagher, N. B.; Bro, R.; Shaver, J. M.; Windig, W.; Koch, R. S. *PLS_Toolbox Version 4.0 for Use with MATLAB*; Eigenvector Research, Inc.: Wenatchee, WA, USA, 2006. http://mitr.p.lodz.pl/raman/jsurmacki/pliki/zajecia/LMDiT/cw3/LMDiT_PLS_Manual_4.pdf.
(36) Næs, T.; Martens, H. Multivariate calibration. II. Chemometric methods. *TrAC, Trends Anal. Chem.* **1984**, *3* (10), 266−271.
(37) de Jong, S.; Wise, B. M.; Ricker, N. L. Canonical partial least squares and continuum power regression. *J. Chemom.* **2001**, *15* (2), 85−100.
(38) Nelson, G. L.; Lackey, H. E.; Bello, J. M.; Felmy, H. M.; Bryan, H. B.; Lamadie, F.; Bryan, S. A.; Lines, A. M. Enabling Microscale Processing: Combined Raman and Absorbance Spectroscopy for Microfluidic On-Line Monitoring. *Anal. Chem.* **2021**, *93* (3), 1643−1651.
(39) Lines, A. M.; Hall, G. B.; Asmussen, S.; Allred, J.; Sinkov, S.; Heller, F.; Gallagher, N.; Lumetta, G. J.; Bryan, S. A. Sensor Fusion: Comprehensive Real-Time, On-Line Monitoring for Process Control via Visible, Near-Infrared, and Raman Spectroscopy. *ACS Sens* **2020**, *5* (8), 2467−2475.
(40) Nelson, G. L.; Lines, A. M.; Bello, J. M.; Bryan, S. A. Online Monitoring of Solutions Within Microfluidic Chips: Simultaneous Raman and UV-Vis Absorption Spectroscopies. *ACS Sens* **2019**, *4* (9), 2288−2295.
(41) Lines, A. M.; Nelson, G. L.; Casella, A. J.; Bello, J. M.; Clark, S. B.; Bryan, S. A. Multivariate Analysis To Quantify Species in the

https://doi.org/10.1021/acsomega.3c06007
ACS Omega 2023, 8, 41696−41707

Presence of Direct Interferents: Micro-Raman Analysis of HNO3 in Microfluidic Devices. *Anal. Chem.* **2018**, *90* (4), 2548−2554.
(42) Tse, P.; Shafer, J.; Bryan, S. A.; Nelson, G. L.; Lines, A. M. Measuring Nd(III) Solution Concentration in the Presence of Interfering Er(III) and Cu(II) Ions: A Partial Least Squares Analysis of Ultraviolet-Visible Spectra. *Appl. Spectrosc.* **2022**, *76* (2), 173−183.

https://doi.org/10.1021/acsomega.3c06007
ACS Omega 2023, 8, 41696−41707